



OPEN

One-pot synthesis of Au-M@SiO₂ (M = Rh, Pd, Ir, Pt) core-shell nanoparticles as highly efficient catalysts for the reduction of 4-nitrophenol

Junfang Hao¹, Bin Liu¹, Shinya Maenosono^{2✉} & Jianhui Yang^{1✉}

The conversion of p-nitrophenol (4-NP) to p-aminophenol (4-AP) is of great significance for pharmaceutical and material manufacturing. In this work, Au-M@SiO₂ (M = Rh, Pd, Ir, Pt) nanoparticles (NPs) with core-shell structures, which are expected to be excellent catalysts for the transformation of 4-NP to 4-AP, were synthesized by a facile one-pot one-step method. The structure and composition of the NPs were characterized through transmission electron microscopy, X-ray powder diffraction and X-ray photoelectron spectroscopy. Au-M@SiO₂ (M = Rh, Pd, Ir, Pt) core-shell NPs showed excellent catalytic activity in the reduction of 4-NP, which is superior to most catalysts reported in the previous literature. The enhanced catalytic activity of Au-M@SiO₂ core-shell NPs is presumably related to the bimetallic synergistic effect. This study provides a simple strategy to synthesize core-shell bimetallic NPs for catalytic applications.

P-nitrophenol (4-NP) is a common organic pollutant, while its reduction product (p-aminophenol, 4-AP) has a wide range of applications in pharmaceuticals, dyestuffs, and high polymer material fields^{1–3}. Therefore, the reduction reaction of 4-NP to 4-AP is of vital practical importance. However, this reaction is very slow without catalyst in the presence of NaBH₄⁴. In recent years, an increasing number of metal catalysts have been used for the reduction of 4-NP. Many investigations have focused on monometallic catalysts, such as Au, Ag, Pd, Cu, Ni and Co^{5–10}. Compared to them, bimetallic catalysts exhibit better catalytic performance, such as Au-Pd alloy nanocrystals, silica (SiO₂)-coated Ag/Au nanoparticles (NPs) and Pt-Rh alloyed nano-multipods^{11–16}. These can be ascribed to their unique morphology and optimized electronic structure by synergy or alloy effects^{17–22}. Au catalysts are widely employed in many fields, for example, CO oxidation, coupling reactions, oxidation of ethanol and degradation of 4-NP, because they are most active and selective under mild or even low-temperature conditions at the nanoscale^{23–26}. Moreover, platinum-group metals (PGMs, such as Rh, Pd, Ir and Pt) have excellent chemical activity and thus exhibit advantageous performance^{27–30}. According to previous reports, bimetallic Au-PGMs nanomaterials have attracted extensive interest for many catalytic applications, such as cyclization reactions, electrocatalysis and CO oxidation^{31–34}. For example, Germano's group reported ultrasmall Au@Pt core-shell nanostructures, which presented an enhanced performance for the hydrogen evolution reaction³⁵. Mu's group synthesized Au/Pd heterojunction@mesoporous SiO₂ yolk-shell nanomaterials that exhibited high stability and plasmon-enhanced catalytic activity³⁶. These results demonstrate that the combination of Au and PGMs is an effective way to enhance their catalytic performance. However, few reports have studied bimetallic Au-PGMs catalysts for the degradation of 4-NP. In addition, only bimetallic NPs tend to aggregate and leach during the reaction progress, resulting in decreased catalytic activity and stability^{37,38}. Therefore, it would be a promising strategy to coat the surface of bimetallic Au-PGMs NPs with a SiO₂ shell to overcome these problems.

In this study, we used a one-pot one-step method to synthesize Au-M@SiO₂ (M = Rh, Pd, Ir, Pt) core-shell NPs. The stability of the catalyst was increased, and the agglomeration of NPs was prevented in the presence

¹Key Laboratory of Synthetic and Natural Functional Molecule Chemistry of Ministry of Education, Shaanxi Key Laboratory of Physico-Inorganic Chemistry, College of Chemistry & Materials Science, Northwest University, Xi'an 710069, People's Republic of China. ²School of Materials Science, Japan Advanced Institute of Science and Technology, 1-1 Asahidai, Nomi, Ishikawa 923-1292, Japan. ✉email: shinya@jaist.ac.jp; jianhui@nwu.edu.cn

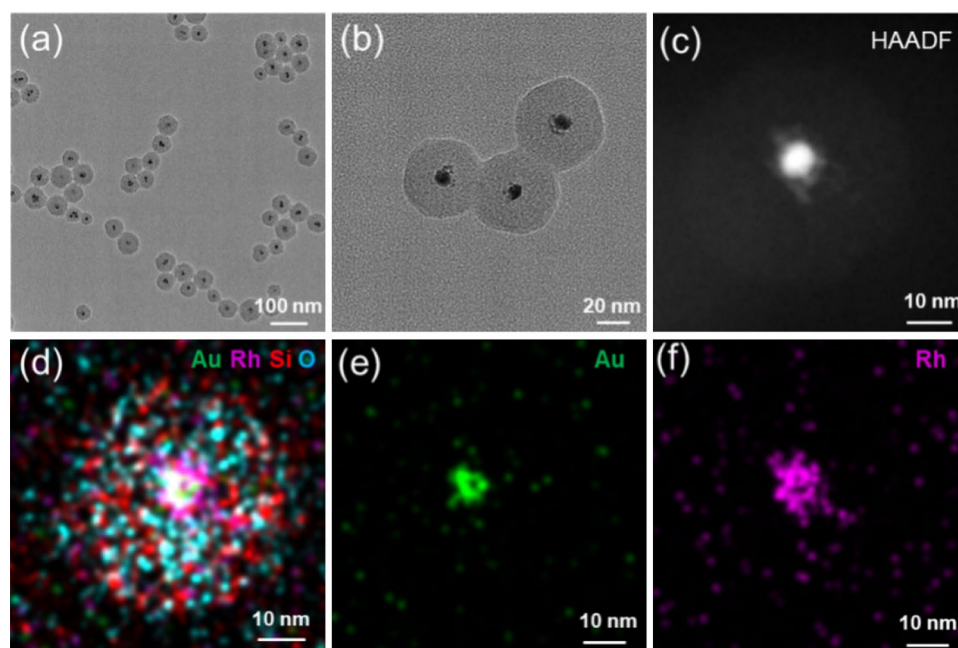


Figure 1. (a, b) TEM, (c) HAADF-STEM and (d–f) elemental mapping images of Au-Rh@SiO₂ core-shell NPs.

of the SiO₂ shell. The morphology and structure of the Au-M@SiO₂ core-shell NPs were determined by TEM, XRD and XPS. The catalytic performance of the Au-M@SiO₂ (M = Rh, Pd, Ir, Pt) core-shell NPs was investigated in the model reaction of the reduction of 4-NP. This work provides a simplified way to prepare SiO₂-coated bimetallic NP catalysts.

Results and discussion

Here, Au-Rh@SiO₂ core-shell NPs are used as an example to illustrate the one-pot synthesis of silica-coated bimetallic Au-M (M = Rh, Pd, Ir and Pt) NPs. The morphology, structure and size of the samples were characterized by TEM. As shown in Fig. 1a,b, the as-prepared sample possesses core-shell structure and good monodispersity. The elemental mapping analysis of the sample in Fig. 1d–f demonstrates that Rh is distributed uniformly in the side of Au, and Au-Rh NPs were coated by silica shell, which further affirms the formation of core-shell structure. It is concluded that Au-Rh@SiO₂ NPs with core-shell structures were synthesized successfully by this one-pot method. Au-Rh@SiO₂ NPs have a core-shell structure. To further clarify the crystalline structure between Au and Rh, Au-Rh NPs synthesized without TEOS were characterized by TEM and high-resolution TEM. As shown in Fig. S1 in the ESM (Electronic Supplementary Material), Au-Rh NPs with core-satellite structure are similar to some Rh “planets” around an Au core. The formation of this unique structure is mainly because of the immiscibility and lattice mismatch of Au and Rh³⁹. There are some heterojunction structures at the boundary between Au and Rh, which could contribute to their electron interaction and further improve their catalytic performance. The mass loading of Au-Rh in Au-Rh@SiO₂ core-shell NPs by chemical method. It is assumed that the precursors HAuCl₄, RhCl₃ and TEOS are completely converted into Au, Rh and SiO₂, respectively. The experimental mass loading of Au-Rh in Au-Rh@SiO₂ core-shell NPs determined by their mass ratio is 7.9%. Au-Rh NPs was obtained by dissolving the silica shell with excess concentrated hydrofluoric acid. The experimental value is slightly smaller than the theoretical value (8.45%) because of the presence of C/TAB in the silica layer.

The crystal structure of Au-Rh@SiO₂ core-shell NPs was obtained by XRD. As shown in Fig. 2a, the main peaks at 38.6°, 45.0°, 65.2°, 78.1°, and 82.8° can be ascribed to the (111), (200), (220), (311), and (222) planes of Au (JCPDS: 04-0784)⁴⁰. These peaks are in accordance with the peak positions of Au@SiO₂ in Fig. S2, indicating the formation of a non-alloyed structure. However, there are no characteristic peaks of Rh. This might be attributed to the fact that the particle size of Rh is too small to be obtained. In addition, a broad peak stemming from the SiO₂ shell is actually seen at around $2\theta \approx 20^\circ$. The elemental composition and states of Au-Rh@SiO₂ core-shell NPs were further analyzed and characterized by XPS, as shown in Fig. 2b. The main peaks of the Rh 3d spectrum can be deconvoluted into four peaks. The two peaks at 304.6 eV and 308.2 eV can be related to Rh 3d_{5/2} and Rh 3d_{3/2} of Rh (0), and those with binding energies of 306.5 eV and 312.2 eV can be related to Rh 3d_{5/2} and Rh 3d_{3/2} of Rh (III)^{41,42}. Compared with the standard values, the peaks of Rh species shift to higher binding energies⁴³. Moreover, through peak area integral calculation, the ratio of Rh (0) and Rh (III) was found to be 1.45. The peak of Au 4f is too weak to clearly observe in the survey-level XPS spectrum (Fig. S3), which is mainly because the Au-Rh “core-satellite” structure is coated by a silica shell⁴⁴. This further confirmed the formation of a heterojunction structure rather than alloy, which is in agreement with the XRD result. The sample of Au-Rh NPs (Fig. S1) synthesized without TEOS was also characterized by XPS. As shown in Fig. S4, Au 4f core-level and Rh 3d core-level signals are present due to the absence of a silica shell. The molar ratio of Au and Rh is

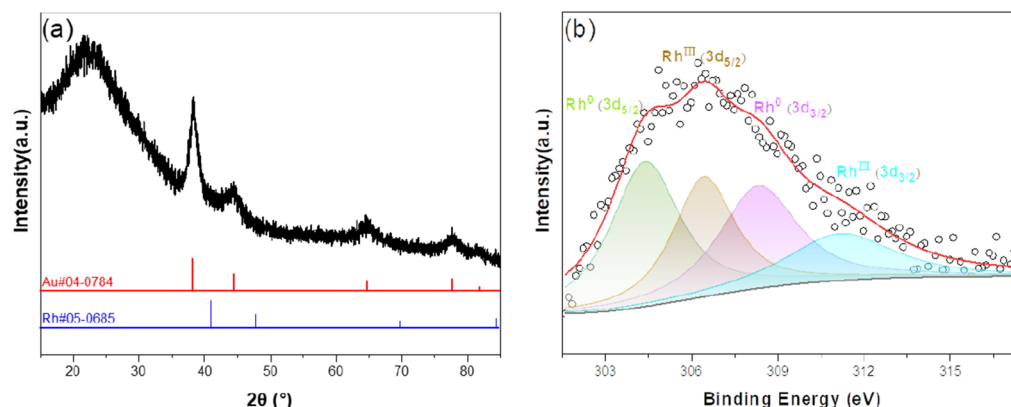


Figure 2. (a) XRD pattern and (b) Rh 3d spectrum of Au-Rh@SiO₂ core-shell NPs.

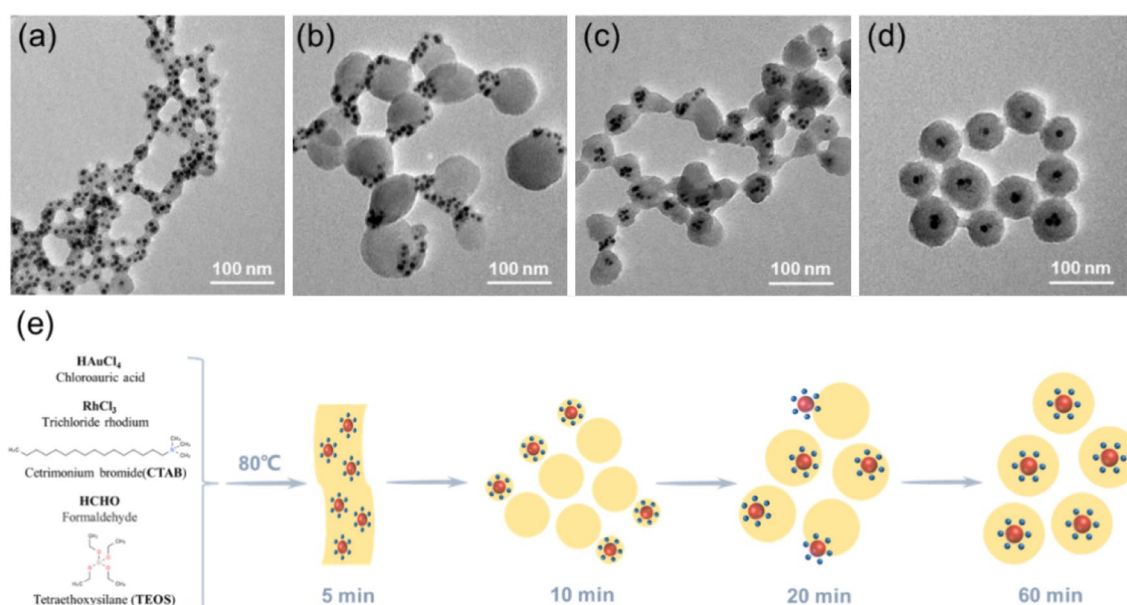


Figure 3. TEM images of the Au-Rh@SiO₂ core-shell NPs at different reaction time: (a) 5 min, (b) 10 min, (c) 20 min and (d) 60 min. The forming process mechanism illustration of Au-Rh@SiO₂ core-shell NPs (e).

1.0 by the calculation of XPS peak areas, which is consistent with that of ICP-MS and the molar ratio of their precursors. In addition, the two peaks of Au (0) shift to the higher binding energy, which is mainly due to the electron interaction between Au and Rh⁴⁵. The electronegativity of Au is higher than that of Rh, which results in an increased electron density of Au and a reduction of electron binding energy. Comparing the XPS spectra of Au-Rh@SiO₂ core-shell and Au-Rh NPs, the ratio of Rh (0) and Rh (III) decreased from 1.45 to 0.75. These observations indicate that Rh NPs are oxidized^{41,43} or the alloy phase generates at the interface between Au and Rh during the XPS measurement^{14–16}. This further revealed that the existence of silica shell could improve their stability.

The formation mechanism of Au-Rh@SiO₂ core-shell NPs was investigated by acquiring TEM images of the samples taken at different reaction times. Here, Au-Rh@SiO₂ core-shell NPs were synthesized by a one-pot one-step method developed by our research group and Zhao's group^{46,47}. HAuCl₄ and RhCl₃ were reduced by formaldehyde to result in the formation of Au-Rh core-satellite NPs after the reacted solution was heated at 80 °C for 5 min. At the same time, a thin layer of silica formed on the surface by base-catalyzed hydrolysis and polymerization of TEOS, as shown in Fig. 3a. In Fig. 3b, most of the Au-Rh NPs coated with a thin silica layer silica are on the outer edge of the silica spheres. The structures of the Au-Rh@SiO₂ core-shell NPs initially formed after 20 min of reaction, as shown in Fig. 3c. However, Au-Rh NPs are not at the center of the silica spheres. At higher concentrations of CTAB, the lamellar micelles formed could induce anisotropic growth of SiO₂ shells on the surface and Au-Rh NPs⁴⁸. As the consumption of CTAB, the spherical micelles adopted may result in the isotropic growth of SiO₂ shells. As shown in Fig. 3d, Au-Rh@SiO₂ core-shell NPs finally formed at 60 min. The forming process mechanism of Au-Rh@SiO₂ core-shell NPs is illustrated in Fig. 3e.

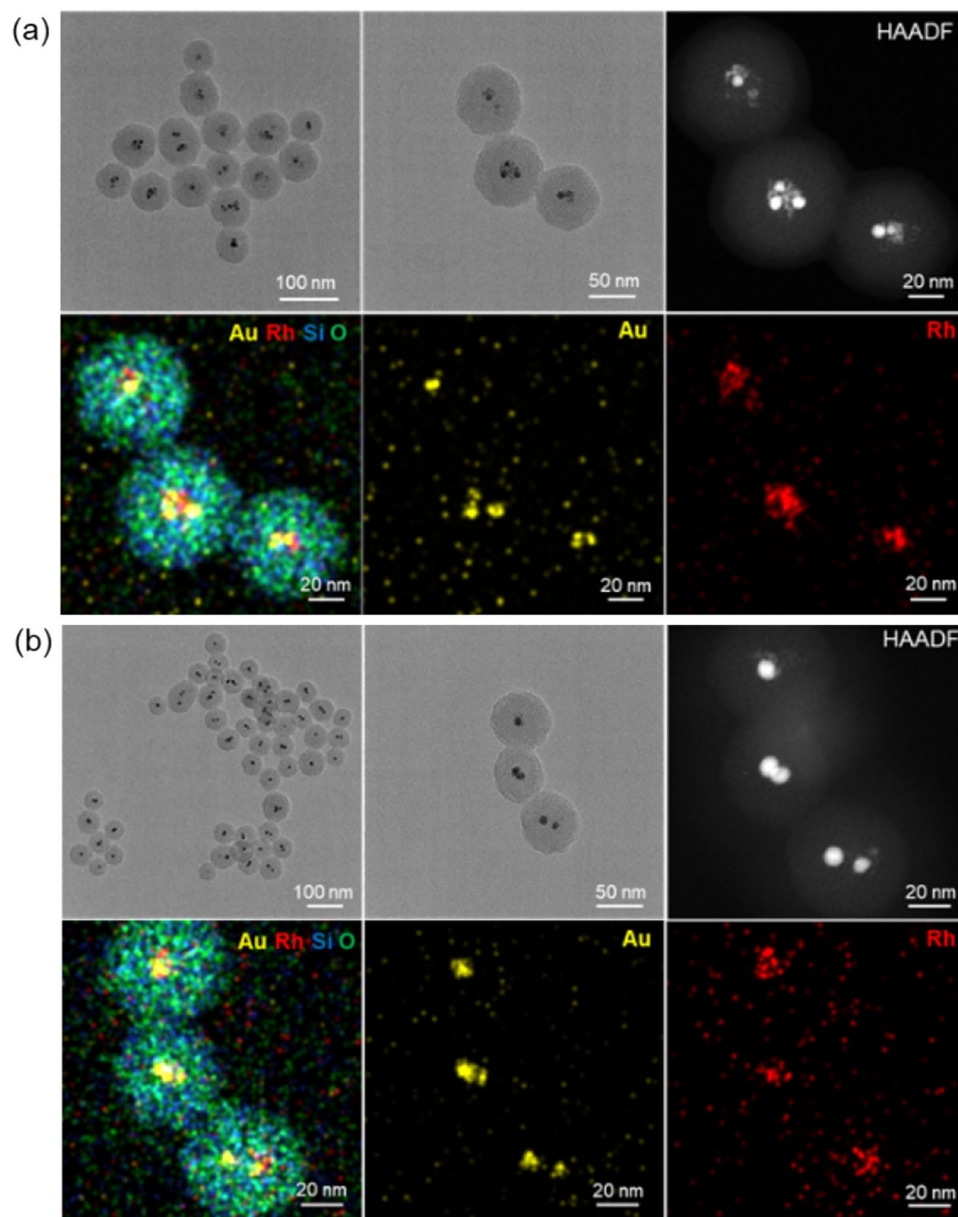


Figure 4. TEM images, HAADF-STEM image, and elemental mapping of (a) $\text{Au}_1\text{-Rh}_2\text{@SiO}_2$ and (b) $\text{Au}_2\text{-Rh}_1\text{@SiO}_2$ core-shell NPs, respectively.

We also investigated the effect of different precursor ratios (1:2 and 2:1) of Au and Rh on the resulting NPs. The samples were defined as $\text{Au}_1\text{-Rh}_2\text{@SiO}_2$ and $\text{Au}_2\text{-Rh}_1\text{@SiO}_2$ core-shell NPs, which were synthesized with HAuCl_4 to RhCl_3 molar ratios of 1:2 and 2:1, respectively. As demonstrated in Fig. 4, the two samples are with core-shell structures, the core is Au-Rh bimetallic NPs, and the shell with similar thickness is silica. When we carefully checked the structure of Au-Rh bimetallic NPs, it could be clearly seen that Au-Rh bimetallic NPs with core-satellite structure and isolated Rh NPs were encapsulated in the center of silica for the $\text{Au}_1\text{-Rh}_2\text{@SiO}_2$ core-shell NPs in Fig. 4a. For $\text{Au}_2\text{-Rh}_1\text{@SiO}_2$ core-shell NPs in Fig. 4b, Au is not coated well with Rh particles and Au-Rh core-satellite structure is not formed in the center of the silica shell. Similarly, we also examined the molar ratio of Au and Rh in $\text{Au}_1\text{-Rh}_2$ and $\text{Au}_2\text{-Rh}_1$ bimetallic NPs without silica shells synthesized in the absence of TEOS by XPS. As shown in Figs. S5 and S6, the molar ratios of Au to Rh of $\text{Au}_1\text{-Rh}_2$ and $\text{Au}_2\text{-Rh}_1$ bimetallic NPs are 0.56 and 1.68 according to the calculation of the corresponding XPS peak areas, respectively.

We also employed this method to synthesize silica-coated bimetallic NPs consisting of Au and other platinum group metals (Pd, Ir, Pt). Figure 5a,b,c shows the TEM image, HAADF-STEM image and elemental mapping of Au-Pd@SiO_2 , Au-Ir@SiO_2 and Au-Pt@SiO_2 core-shell NPs, respectively. Combined with the results of TEM and XRD characterizations of Au-Pd, Au-Ir and Au-Pt bimetallic NPs shown in Figs. S7 and S8, Au-Pd@SiO_2 , Au-Ir@SiO_2 and Au-Pt@SiO_2 core-shell NPs can be successfully synthesized using this one-pot one-step method simply by changing the corresponding metallic precursor.

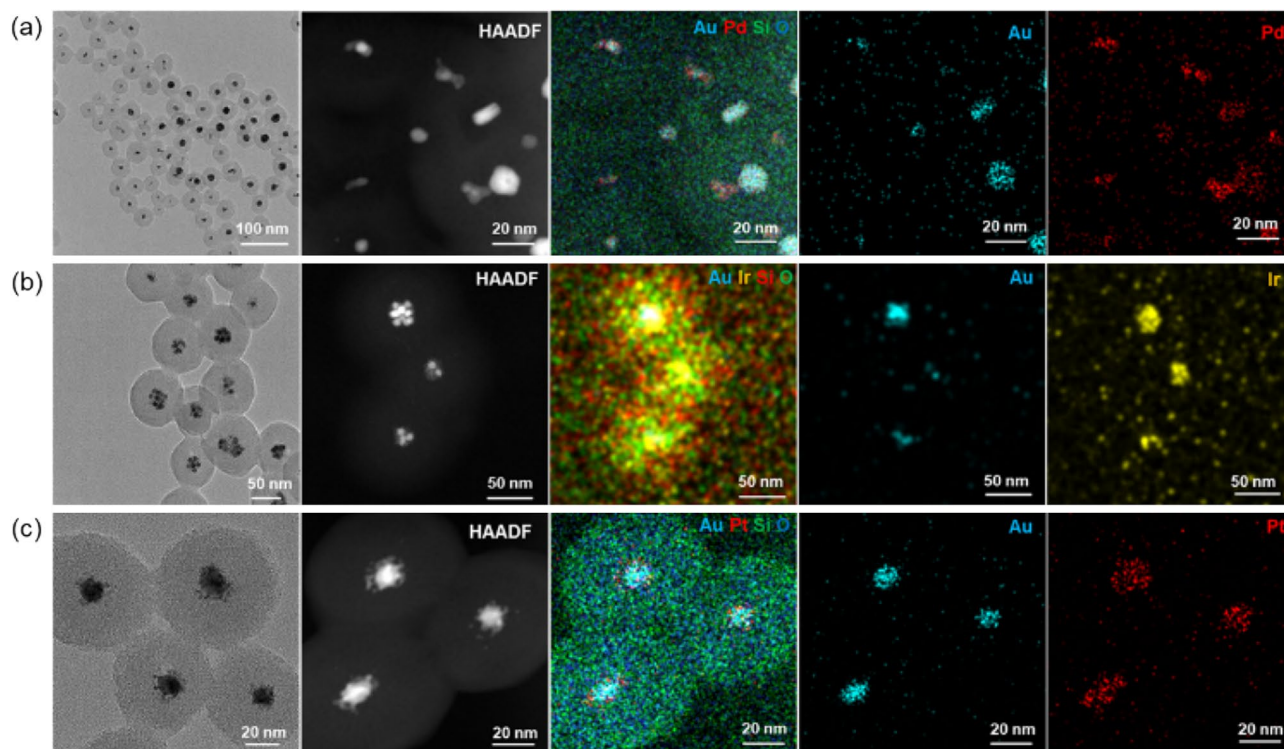


Figure 5. TEM image, HAADF-STEM image and elemental mapping of (a) Au-Pd@SiO₂, (b) Au-Ir@SiO₂ and (c) Au-Pt@SiO₂ core-shell NPs, respectively.

To explore the catalytic reduction performance of 4-NP to 4-AP, UV-vis spectra in the presence of NaBH₄ during different reaction times were monitored. The UV-vis absorption peaks of 4-NP and 4-AP are located at 400 nm and 300 nm in Fig. S9, respectively. The UV-vis spectra of Au-Rh@SiO₂ core-shell NPs as a catalyst in Fig. 6a show that the reduction reaction of 4-NP finished within 5 min, indicating its good catalytic performance. The catalytic capability of Rh@SiO₂ (Fig. S10a), Au@SiO₂, and the mixture was further measured. Distinctly, in Fig. 6b–d, in the presence of Rh@SiO₂, Au@SiO₂ and the mixture as a catalyst, this reaction finished within 8 min, 60 min and 13 min, respectively. The broad peak at approximately 500–550 nm comes from the surface resonance plasmon resonance of Au NPs (Fig. S11). This phenomenon exhibits that Au-Rh@SiO₂ core-shell NPs feature superior catalytic performance over their corresponding single component catalysts.

In addition, the investigation on kinetics of the catalysts were further analyzed. If the ratio of C_t/C_0 (4-NP concentration at t minutes and 0 min) is proportional to time, this reduction reaction could be seen as first order kinetic, and the slope of the fitting line is a first order kinetic constant⁴⁹. The corresponding results are shown in Fig. 7. The first-order kinetic constants of Au-Rh@SiO₂ core-shell NPs, Rh@SiO₂, Au@SiO₂ and the mixture of Rh@SiO₂ and Au@SiO₂ NPs as catalysts are 0.826 min⁻¹, 0.276 min⁻¹, 0.037 min⁻¹ and 0.228 min⁻¹, respectively. Clearly, Au-Rh@SiO₂ core-shell NPs have the maximum kinetic constant, also suggesting that this material exhibits the best catalytic performance. In addition, it can be observed from Table 1 that this catalyst is also superior to other bimetallic nanocatalysts reported in the previous literature^{1,12,50–53}, revealing its excellent catalytic activity.

According to the results of TEM and XPS characterization of the Au-Rh@SiO₂ core-shell NPs, Au-Rh bimetallic NPs exhibit core-satellite structures. There are some heterojunction structures at the boundary between Au and Rh, which result in their electron interaction and could improve their catalytic performance. To verify our hypothesis, the catalytic performance of Au-Rh@SiO₂ core-shell NPs with different molar ratios of Au and Rh in Figs. S12 and S13 show UV-vis spectra at different reaction times in the presence of Au₁-Rh₂@SiO₂ core-shell NPs and Au₂-Rh₁@SiO₂ core-shell NPs. Figure 8 plots $\ln(C_t/C_0)$ versus time in the presence of Au-Rh@SiO₂ core-shell NPs with different molar ratios of Au and Rh. Compared with the kinetic constant of Au-Rh@SiO₂ core-shell NPs, Au₂-Rh₁@SiO₂ core-shell NPs exhibited the lowest catalytic performance due to the low content of Rh. However, for the sample of Au₁-Rh₂@SiO₂ core-shell NPs, its catalytic performance was still lower than that of Au-Rh@SiO₂ core-shell NPs. As observed in Fig. 3a, a thicker layer of Rh NPs was formed and prevented the synergistic effect of Au and Rh. In conclusion, the Au-Rh@SiO₂ core-shell NPs as highly efficient catalysts for the reduction of 4-NP could be attributed to the synergistic effect coming from their unique core-shell structure and electronic interaction of Au and Rh.

The synergistic effect was also confirmed by other silica-coated Au-based PGMs bimetallic NPs. Figs. S14, S15, S16 and S17 show the catalytic performance of Au-M@SiO₂ (M = Pd, Ir, Pt) core-shell NPs for the reduction of 4-NP. They exhibit highly efficient catalytic activity with first-order kinetic constants of 0.359 min⁻¹, 0.100 min⁻¹ and 0.135 min⁻¹, respectively. As shown in Fig. 9, we summarized the Au-M@SiO₂ (M = Rh, Pd, Ir, Pt) core-shell NPs as catalysts for the reduction of 4-NP. Au-Rh@SiO₂ core-shell NPs exhibit the highest catalytic activity

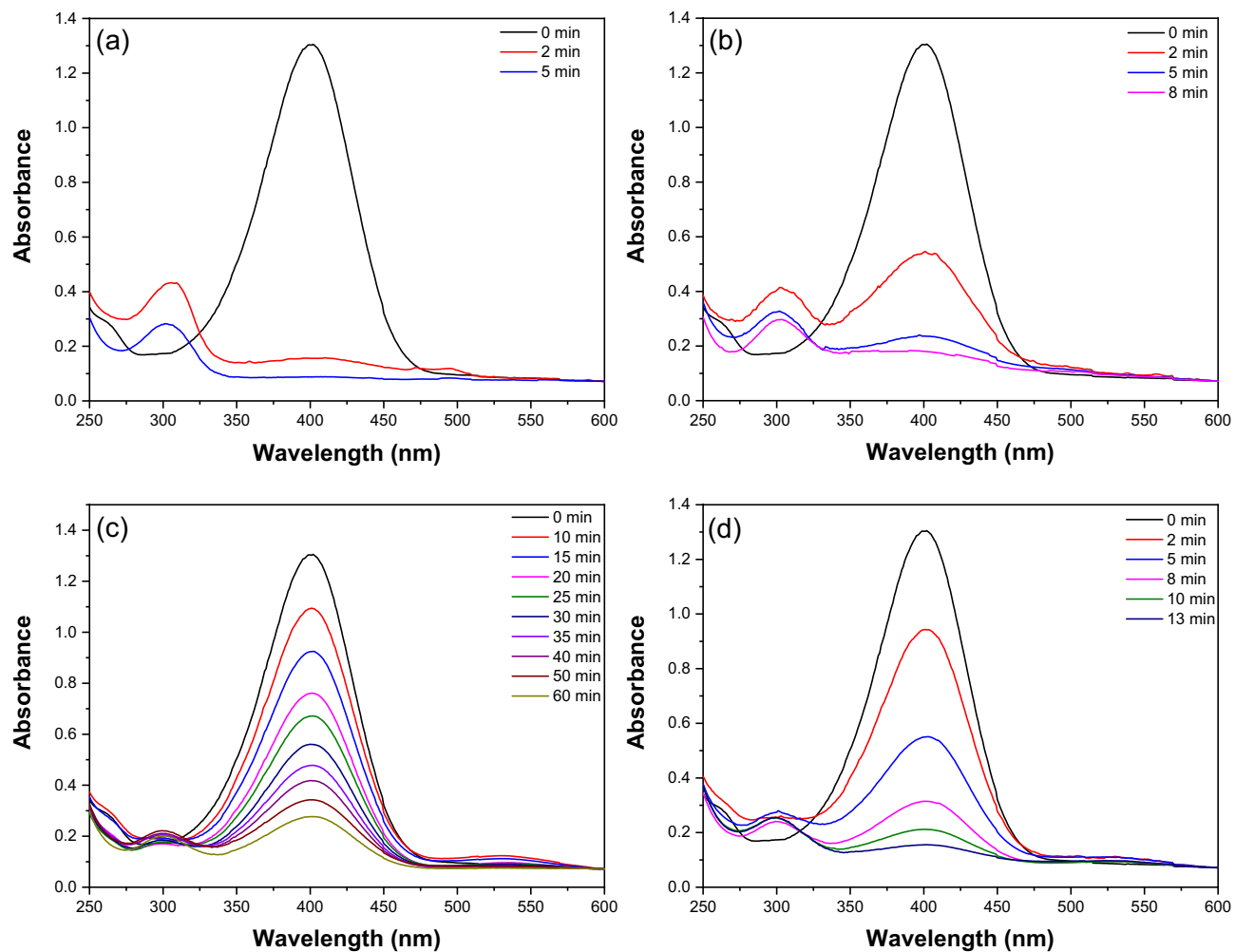


Figure 6. UV-vis spectra at different reaction times in the presence of Au-Rh@SiO₂ core-shell NPs (a), Rh@SiO₂ core-shell NPs (b), Au@SiO₂ core-shell NPs (c) and the mixture of Rh@SiO₂ and Au@SiO₂ core-shell NPs (d), respectively.

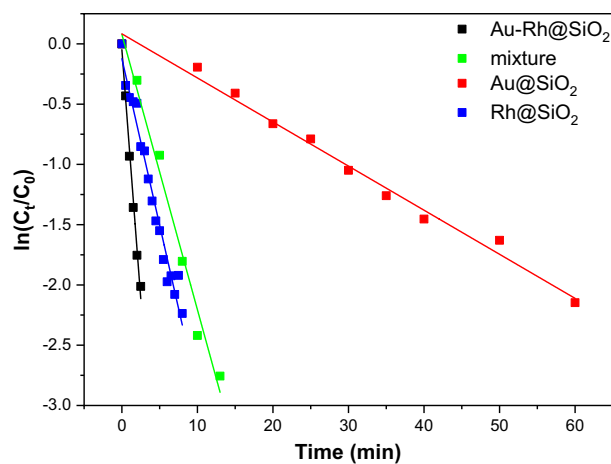


Figure 7. Plots of $\ln(C_t/C_0)$ versus time in the presence of Au-Rh@SiO₂ core-shell NPs, Rh@SiO₂ core-shell NPs, Au@SiO₂ core-shell NPs and the mixture of Rh@SiO₂ and Au@SiO₂ core-shell NPs as catalysts.

Catalyst	Mass	Kinetic constant	References
MOF-supported Au@Ag core-shell NPs	–	0.298 min ⁻¹	12
Au/Pd core-shell nanocubes	1 mL of 4.2 × 10 ¹⁰ particle/mL	2.05 ± 0.12 min ⁻¹	50
Ni-Pt NPs	1 mL of 0.1 mg/mL	0.116 min ⁻¹	51
Pd/Au(3:1)@g-C ₃ N ₄ -N	–	0.5310 min ⁻¹	52
Au/Pd core/shell NPs	75 μL of 2.0 mM	0.32 min ⁻¹	1
Cu/Ag alloy NPs	2 mg	0.237 min ⁻¹	53
Au-Rh@SiO ₂ core-shell structure	1 mL of 0.019 mg/mL	0.826 min ⁻¹	This work

Table 1. Comparison of catalytic performance of bimetallic nanocatalysts for the reduction of 4-NP.

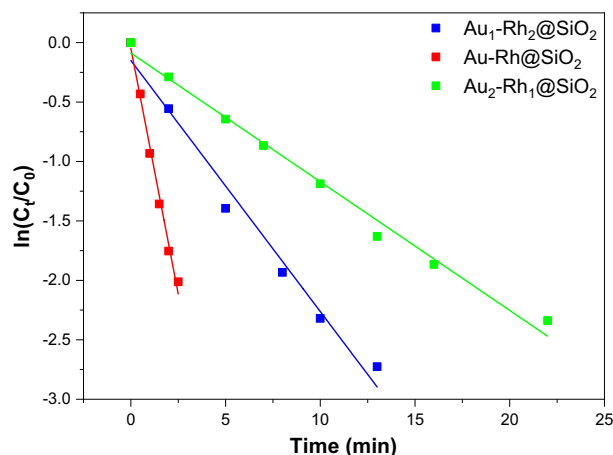


Figure 8. Plots of ln(C_t/C₀) versus time in the presence of Au₁-Rh₂@SiO₂ core-shell NPs, Au-Rh@SiO₂ core-shell NPs, Au₂-Rh₁@SiO₂ core-shell NPs.

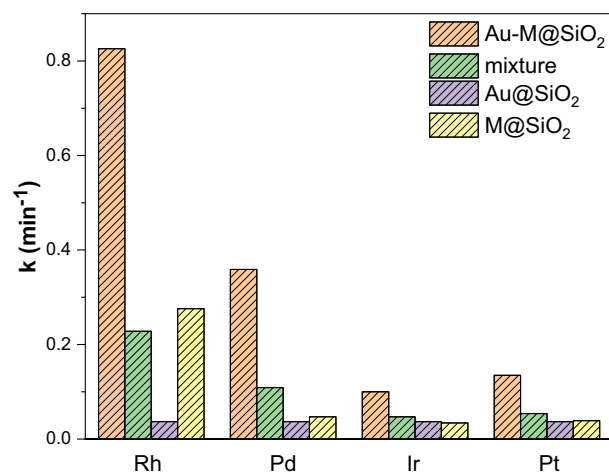


Figure 9. The catalytic performance of Au-M@SiO₂ (M = Rh, Pd, Ir, Pt) core-shell NPs for reduction of 4-NP.

for the reduction of 4-NP in the excess of NaBH₄, which is due to the higher adsorption energy of 4-NP on Rh surfaces and more efficient interfacial electron transfer between Au and Rh.

The recyclability of Au-Rh@SiO₂ core-shell NPs shown in Fig. 10 demonstrates that the conversion rate is still around 90% after 5 cycles, indicating its high stability. As shown in Fig. S18, the first-order kinetic constant of Au-Rh NPs to the reduction reaction is 0.807 min⁻¹, which is slightly lower than that (0.826 min⁻¹) of Au-Rh@SiO₂ core-shell NPs. As observed in Fig. S19, Au-Rh bimetallic NPs occurs obvious agglomeration after catalysis three times. The conversion rate of Au-Rh bimetallic NPs after catalysis three times reduced to 79%. On the

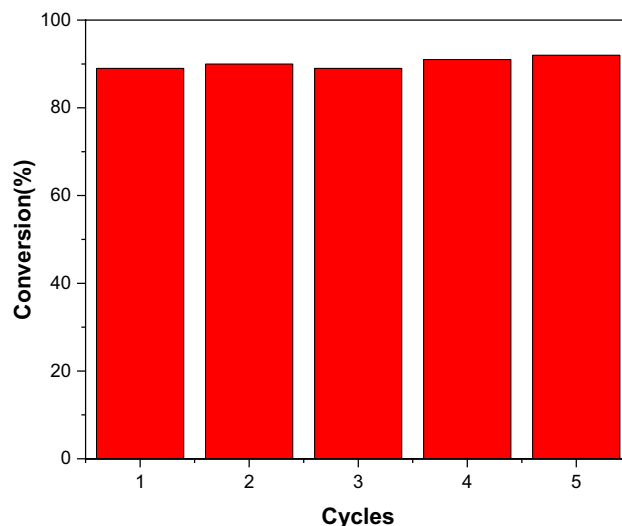


Figure 10. The conversion rate for different cycles of Au-Rh@SiO₂ core-shell NPs for reduction of 4-NP.

contrary, Au-Rh@SiO₂ core-shell NPs still can keep the original morphology and structure after five cycles of catalysis. It illustrates that SiO₂ shell layers can improve the stability.

Therefore, the highly efficient catalytic performance of Au-Rh@SiO₂ core-shell NPs mainly comes from the synergistic effect of Au-Rh and core-shell structure. The catalytic performance of Au-Rh@SiO₂ core-shell NPs is superior to that of the corresponding monometallic@SiO₂ NPs or their mixture. TEM and XPS characterizations indicate the formation of heterojunction structures at the boundary of Au-Rh and their electron interaction. The electron interaction is insufficient as decreasing the molar ratio of Rh/Au and is hindered as increasing the molar ratio of Rh/Au. It sufficiently demonstrates the synergistic effect of Au-Rh results in the highly efficient catalytic performance for the reduction of 4-NP. The SiO₂ shell layer improves their high catalytic cycle stability and recovery.

Conclusions

In summary, Au-M@SiO₂ (M = Rh, Pd, Ir, Pt) NPs with core-shell structures were successfully synthesized by a facile one-pot one-step method. The morphology, crystal structure, elemental composition and formation mechanism of these core-shell NPs were investigated. Au-M@SiO₂ (M = Rh, Pd, Ir, Pt) core-shell NPs showed excellent catalytic activity in the reduction of 4-NP, which is superior to most catalysts reported in the previous literature. The enhanced catalytic activity of Au-M@SiO₂ core-shell NPs is presumably related to the bimetallic synergistic effect. This study provides a simple strategy to synthesize core-shell bimetallic NPs for catalytic applications.

Methods

Materials. Chloroauric acid tetrahydrate (HAuCl₄·4H₂O, > 47.0%, Beijing Huawei Ruike Chemical Co., Ltd), palladium chloride acid (H₂PdCl₄, > 97.0%, Shanghai Macklin Biochemical Co., Ltd), chloroplatinic acid hexahydrate (H₂PtCl₆·6H₂O, ≥ 37.0%, Shanghai Institute of Fine Chemical Materials), rhodium chloride trihydrate (RhCl₃·3H₂O, ≥ 39.0%, Xi'an Kaili Chemical Co., Ltd), cetyltrimethylammonium bromide (CTAB, C₁₉H₄₂BrN, 97.0%, Shanghai Macklin Biochemical Co., Ltd), iridium trichloride (IrCl₃, ≥ 42.5%, Shanghai Bide Pharmaceutical Technology Co., Ltd), sodium hydroxide (NaOH, ≥ 96.0%, Tianjin Tianli Chemical Reagent Co., Ltd), formaldehyde solution (HCHO, 37.0%–40.0%, Tianjin Fuyu Chemical Reagent Co., Ltd), 4-NP (C₆H₅NO₂, 99%, Damas-beta Reagent Co., Ltd), sodium borohydride (NaBH₄, Tianjin Cameo Chemical Reagent Co., Ltd.) and tetraethyl orthosilicate (TEOS, Tianjin Cameo Chemical Reagent Co., Ltd.) were directly used without further purification. Anhydrous alcohol and deionized water were used in all experiments.

Synthesis. Au@SiO₂ core-shell NPs were synthesized by a facile one-pot one-step method using formaldehyde as a reducing agent^{46,47}. Similarly, M@SiO₂ (M = Rh, Pd, Ir and Pt) core-shell NPs were prepared by changing the corresponding metal precursors.

The above method is still suitable for the synthesis of bimetallic Au-M@SiO₂ (M = Rh, Pd, Ir and Pt) core-shell NPs. Taking Au-Rh@SiO₂ core-shell NPs as an example, in a typical synthesis, 38 mL of deionized water, 6 mL of ethanol, 0.07 g of CTAB, 1 mL of HCHO, 1 mL of NaOH (0.5 mol/L), 1 mL of 8.14 mmol/L HAuCl₄, 1 mL of 8.14 mmol/L RhCl₃ and 0.10 mL of TEOS were mixed in a 100 mL of beaker under ultrasonication. The beaker was left in an oil bath at 80 °C for 60 min under stirring. After cooling to room temperature naturally, the product was centrifuged at 11,000 rpm for 20 min and washed two times with water to remove the surfactant and unreacted chemicals. Finally, the precipitate was dissolved in 3 mL of water for further characterization.

Au-Rh@SiO₂ core-shell NPs with different Au/Rh molar ratios were obtained under the same reaction conditions by changing the molar ratio of HAuCl₄ to RhCl₃ to 1:2 and 2:1, respectively.

The other Au-M@SiO₂ (M = Pd, Ir and Pt) core-shell NPs were prepared by replacing RhCl₃ with H₂PdCl₄, RhCl₃ and H₂PtCl₆, respectively.

The procedure of preparing Au-M (M = Rh, Pd, Ir and Pt) bimetallic NPs is similar to the typical synthesis of Au-Rh@SiO₂ core-shell NPs in the absence of TEOS.

Characterization. Transmission electron microscopy (TEM) images were obtained from Talos F200X (FEI, 200 kV) equipped with a high-angle annular dark field (HAADF) detector and an energy dispersive X-ray (EDX) spectrometer. The TEM samples were prepared by dropping nanoparticle dispersions onto 200-mesh copper grids covered with carbon membranes. X-ray diffraction (XRD) measurements were carried out on a Bruker D8 Advance diffractometer with Cu K α radiation ($\lambda = 1.54059 \text{ \AA}$). X-ray photoelectron spectrophotometer (XPS) spectra were taken by using a PHI5000 Versa Probe III spectrometer with an excitation source of Al K α . The samples for XRD and XPS were prepared by dropping nanoparticle dispersion onto silicon wafers and dried naturally at room temperature. All spectra were recalibrated with respect to the C 1 s core level peak at 284.8 eV of carbon contamination. UV-vis absorption spectra were obtained on an ultraviolet-visible spectrophotometer (SP-75). The element ratio was determined by inductively coupled plasma-mass spectrometry (ICP-MS, Agilent 7900).

Catalytic reduction of 4-nitrophenol. 1 mL of freshly prepared NaBH₄ (0.06 mol/L) was mixed with 1 mL of 4-NP (1.7×10^{-4} mol/L) in a quartz cuvette with 1 cm path length. The detailed illustration takes Au-Rh@SiO₂ NPs as an example. 1 mL of Au-M@SiO₂ core-shell NP aqueous dispersion was quickly added to the above solution. The catalytic reaction progress of the conversion of 4-NP to 4-AP was observed via UV-vis spectroscopy between 250 and 600 nm at ambient temperature.

Data availability

The datasets used and/or analysed during the current study available from the corresponding author on reasonable request. All data generated or analysed during this study are included in this published article and its supplementary information files.

Received: 9 March 2022; Accepted: 28 April 2022

Published online: 10 May 2022

References

- Srisombat, L., Nonkumwong, J., Suwannarat, K., Kuntalue, B. & Ananta, S. Simple preparation Au/Pd core/shell nanoparticles for 4-nitrophenol reduction. *Colloids Surf. A Physicochem. Eng. Asp.* **512**, 17–25 (2017).
- Serrà, A., Artal, R., Pozo, M., García-Amorós, J. & Gómez, E. Simple environmentally-friendly reduction of 4-nitrophenol. *Catalysts* **10**, 458–469 (2020).
- Wang, Y. N. *et al.* One-pot green synthesis of bimetallic hollow palladium-platinum nanotubes for enhanced catalytic reduction of p-nitrophenol. *J. Colloid Interface Sci.* **539**, 161–167 (2019).
- Zhao, P. X., Feng, X. W., Huang, D. S., Yang, G. Y. & Astruc, D. Basic concepts and recent advances in nitrophenol reduction by gold- and other transition metal nanoparticles. *Coord. Chem. Rev.* **287**, 114–136 (2015).
- Lin, F. H. & Doong, R. A. Highly efficient reduction of 4-nitrophenol by heterostructured gold-magnetite nanocatalysts. *Appl. Catal. A Gen.* **486**, 32–41 (2014).
- Dubey, S. P. *et al.* Synthesis of graphene-carbon sphere hybrid aerogel with silver nanoparticles and its catalytic and adsorption applications. *Chem. Eng. J.* **244**, 160–167 (2014).
- Liu, T. *et al.* Pd nanoparticle-decorated 3D-printed hierarchically porous TiO₂ scaffolds for the efficient reduction of a highly concentrated 4-nitrophenol solution. *ACS Appl. Mater. Interfaces* **12**, 28100–28109 (2020).
- Jia, W. L. *et al.* Nitrogen-doped porous carbon-encapsulated copper composite for efficient reduction of 4-nitrophenol. *J. Colloid Interface Sci.* **594**, 254–264 (2021).
- Jiang, Z. F., Xie, J. M., Jiang, D. L., Wei, X. J. & Chen, M. Modifiers-assisted formation of nickel nanoparticles and their catalytic application to p-nitrophenol reduction. *CrystEngComm* **15**, 560–569 (2013).
- Zhang, Y. X. *et al.* Active cobalt induced high catalytic performances of cobalt ferrite nanobrushes for the reduction of p-nitrophenol. *J. Colloid Interface Sci.* **535**, 499–504 (2019).
- Zhang, J. W. *et al.* Surfactant-concentration-dependent shape evolution of Au-Pd alloy nanocrystals from rhombic dodecahedron to trisoctahedron and hexoctahedron. *Small* **9**, 538–544 (2013).
- Jiang, H. L., Akita, T., Ishida, T., Haruta, M. & Xu, Q. Synergistic catalysis of Au@Ag core-shell nanoparticles stabilized on metal-organic framework. *J. Am. Chem. Soc.* **133**, 1304–1306 (2011).
- Chen, Y., Wang, Q. H. & Wang, T. M. Fabrication of thermally stable and active bimetallic Au-Ag nanoparticles stabilized on inner wall of mesoporous silica shell. *Dalton Trans.* **42**, 13940–13947 (2013).
- Zhu, X. Y. *et al.* Controlled fabrication of well-dispersed AgPd nanoclusters supported on reduced graphene oxide with highly enhanced catalytic properties towards 4-nitrophenol reduction. *J. Colloid Interface Sci.* **516**, 355–363 (2018).
- Zhang, X. F., Zhu, X. Y., Feng, J. J. & Wang, A. J. Solvothermal synthesis of N-doped graphene supported PtCo nanodendrites with highly catalytic activity for 4-nitrophenol reduction. *Appl. Surf. Sci.* **428**, 798–808 (2018).
- Yan, Q., Wang, X. Y., Feng, J. J., Mei, L. P. & Wang, A. J. Simple fabrication of bimetallic platinum-rhodium alloyed nano-multipods: a highly effective and recyclable catalyst for reduction of 4-nitrophenol and rhodamine B. *J. Colloid Interface Sci.* **582**, 701–710 (2021).
- Ma, T., Liang, F., Chen, R. S., Liu, S. M. & Zhang, H. J. Synthesis of Au-Pd bimetallic nanoflowers for catalytic reduction of 4-nitrophenol. *Nanomaterials* **7**, 239–247 (2017).
- Zhang, H. J. & Toshima, N. Synthesis of Au/Pt bimetallic nanoparticles with a Pt-rich shell and their high catalytic activities for aerobic glucose oxidation. *J. Colloid Interface Sci.* **394**, 166–176 (2013).
- Patnaik, S., Sahoo, D. P. & Parida, K. M. Bimetallic co-effect of Au-Pd alloyed nanoparticles on mesoporous silica modified g-C₃N₄ for single and simultaneous photocatalytic oxidation of phenol and reduction of hexavalent chromium. *J. Colloid Interface Sci.* **560**, 519–535 (2020).

20. Pozun, Z. D. *et al.* A systematic investigation of p-nitrophenol reduction by bimetallic dendrimer encapsulated nanoparticles. *J. Phys. Chem. C* **117**, 7598–7604 (2013).
21. Suwannarat, K., Thongthai, K., Ananta, S. & Srisombat, L. Synthesis of hollow trimetallic Ag/Au/Pd nanoparticles for reduction of 4-nitrophenol. *Colloids Surf. A Physicochem. Eng. Asp.* **540**, 73–80 (2018).
22. Endo, T., Yoshimura, T. & Esumi, K. Synthesis and catalytic activity of gold-silver binary nanoparticles stabilized by PAMAM dendrimer. *J. Colloid Interface Sci.* **286**, 602–609 (2005).
23. Shanmugaraj, K., Bustamante, T. M., Torres, C. C. & Campos, C. H. Gold nanoparticles supported on mesostructured oxides for the enhanced catalytic reduction of 4-nitrophenol in water. *Catal. Today* **388–389**, 383–393 (2020).
24. Seo, Y. S. *et al.* Catalytic reduction of 4-nitrophenol with gold nanoparticles synthesized by caffeic acid. *Nanoscale Res. Lett.* **12**, 7–17 (2017).
25. Li, F., Zhou, H. P., Fan, J. J. & Xiang, Q. J. Amine-functionalized graphitic carbon nitride decorated with small-sized Au nanoparticles for photocatalytic CO₂ reduction. *J. Colloid Interface Sci.* **570**, 11–19 (2020).
26. Sarkodie, B. *et al.* Highly efficient Au/Fe₂O₃ for CO oxidation: the vital role of spongy Fe₂O₃ toward high catalytic activity and stability. *J. Colloid Interface Sci.* **608**, 2181–2191 (2022).
27. Yang, Y. *et al.* NIR-II driven plasmon-enhanced catalysis for a timely supply of oxygen to overcome hypoxia-induced radiotherapy tolerance. *Angew. Chem. Int. Ed.* **58**, 15069–15075 (2019).
28. Oh, H. S., Nong, H. N., Reier, T., Gliech, M. & Strasser, P. Oxide-supported Ir nanodendrites with high activity and durability for the oxygen evolution reaction in acid PEM water electrolyzers. *Chem. Sci.* **6**, 3321–3328 (2015).
29. Wang, J. *et al.* One-step and rapid synthesis of “clean” and monodisperse dendritic Pt nanoparticles and their high performance toward methanol oxidation and p-nitrophenol reduction. *Nanoscale* **4**, 1549–1552 (2012).
30. Guo, Y. *et al.* Pore structure dependent activity and durability of mesoporous rhodium nanoparticles towards the methanol oxidation reaction. *Chem. Commun.* **56**, 4448–4451 (2020).
31. Du, C. *et al.* Epitaxial growth of zigzag PtAu alloy surface on Au nano-pentagons with enhanced Pt utilization and electrocatalytic performance toward ethanol oxidation reaction. *Electrochim. Acta* **238**, 263–268 (2017).
32. Lv, F. *et al.* A convenient detection system consisting of efficient Au@PtRu nanozymes and alcohol oxidase for highly sensitive alcohol biosensing. *Nanoscale Adv.* **2**, 1583–1589 (2020).
33. Liang, Z. X. *et al.* Direct 12-electron oxidation of ethanol on a ternary Au(core)-PtIr(Shell) electrocatalyst. *J. Am. Chem. Soc.* **141**, 9629–9636 (2019).
34. Wagh, S. B., Hsu, Y. C. & Liu, R. S. Two distinct cyclizations of 2-propenyl-1-ethynyl benzenes with aryldiazo esters using Au and Rh/Au catalysts respectively. *ACS Catal.* **6**, 7160–7166 (2016).
35. Germano, L. D., Marangoni, V. S., Mogili, N. V. V., Seixas, L. & Maroneze, C. M. Ultrasmall (< 2 nm) Au@Pt nanostructures: tuning the surface electronic states for electrocatalysis. *ACS Appl. Mater. Interfaces* **11**, 5661–5667 (2019).
36. Mu, Y. J., Zhang, H. Y., Zheng, W. T. & Cui, X. Q. Highly stable Au/Pd@mesoporous SiO₂ yolk-shell hetero-nanostructures for plasmon-enhanced visible light driven catalytic reactions. *New J. Chem.* **41**, 786–792 (2017).
37. Bahadur, N. M. *et al.* Rapid one-step synthesis, characterization and functionalization of silica coated gold nanoparticles. *Colloids Surf. A Physicochem. Eng. Asp.* **392**, 137–144 (2011).
38. Lee, I., Joo, J. B., Yin, Y. D. & Zaera, F. A yolk@shell nanoarchitecture for Au/TiO₂ catalysts. *Angew. Chem. Int. Ed.* **50**, 10208–10211 (2011).
39. Piccolo, L. *et al.* Understanding and controlling the structure and segregation behaviour of AuRh nanocatalysts. *Sci. Rep.* **6**, 35226 (2016).
40. Huang, J. S., Han, X. Y., Wang, D. W., Liu, D. & You, T. Y. Facile synthesis of dendritic gold nanostructures with hyperbranched architectures and their electrocatalytic activity toward ethanol oxidation. *ACS Appl. Mater. Interfaces* **5**, 9148–9154 (2013).
41. Tabet-Aoul, A., Wang, H. X., Wang, Y. L. & Mohamedi, M. 3D porous sphere-like aggregates of bimetallic PtRh nanoparticles grown onto carbon nanotubes: efficient and durable catalyst for the ethanol oxidation reaction. *J. Electrochem. Soc.* **164**, F685–F693 (2017).
42. Meng, X. Y. *et al.* Distance synergy of MoS₂-confined rhodium atoms for highly efficient hydrogen evolution. *Angew. Chem. Int. Ed.* **59**, 10502–10507 (2020).
43. Bai, J., Xing, S. H., Zeng, J. H., Jiang, J. X. & Chen, Y. Hydrothermal synthesis and catalytic application of ultrathin rhodium nanosheet nanoassemblies. *ACS Appl. Mater. Interfaces* **8**, 33635–33641 (2016).
44. Liu, Y. S., Zhang, W., Li, X. L., Le, X. D. & Ma, J. T. Catalysis of the hydro-dechlorination of 4-chlorophenol and the reduction of 4-nitrophenol by Pd/Fe₃O₄@SiO₂/m-SiO₂. *New J. Chem.* **39**, 6474–6481 (2015).
45. Wang, H. *et al.* Mesoporous bimetallic Au@Rh core-shell nanowires as efficient electrocatalysts for pH-universal hydrogen evolution. *ACS Appl. Mater. Interfaces* **13**, 30479–30485 (2021).
46. Chen, J. C., Zhang, R. Y., Han, L., Tu, B. & Zhao, D. Y. One-pot synthesis of thermally stable gold@mesoporous silica core-shell nanospheres with catalytic activity. *Nano Res.* **6**, 871–879 (2013).
47. Zhang, S., Xu, X. C., Zhang, G. Y., Liu, B. & Yang, J. H. One-pot one-step synthesis of Au@SiO₂ core-shell nanoparticles and their shell-thickness-dependent fluorescent properties. *RSC Adv.* **9**, 17674–17678 (2019).
48. Vega, M. S., Martinez, A. G. & Cucinotta, F. Facile strategy for the synthesis of Gold@silica hybrid nanoparticles with controlled porosity and Janus morphology. *Nanomaterials* **9**, 348–366 (2019).
49. Hu, H. W., Xin, J. H., Hu, H. & Wang, X. W. Structural and mechanistic understanding of an active and durable graphene carbocatalyst for reduction of 4-nitrophenol at room temperature. *Nano Res.* **8**, 3992–4006 (2015).
50. Cui, Y. *et al.* Atomic-level insights into strain effect on p-nitrophenol reduction via Au@Pd core-shell nanocubes as an ideal platform. *J. Catal.* **381**, 427–433 (2020).
51. Ghosh, S. K., Mandal, M., Kundu, S., Nath, S. & Pal, T. Bimetallic Pt-Ni nanoparticles can catalyze reduction of aromatic nitro compounds by sodium borohydride in aqueous solution. *Appl. Catal. A Gen.* **268**, 61–66 (2004).
52. Fang, W. *et al.* Synthesis of Pd/Au bimetallic nanoparticle-loaded ultrathin graphitic carbon nitride nanosheets for highly efficient catalytic reduction of p-nitrophenol. *J. Colloid Interface Sci.* **490**, 834–843 (2017).
53. Wu, W. *et al.* A one-pot route to the synthesis of alloyed Cu/Ag bimetallic nanoparticles with different mass ratios for catalytic reduction of 4-nitrophenol. *J. Mater. Chem. A* **3**, 3450–3455 (2015).

Acknowledgements

This work was supported by the Education Commission of Shaanxi Province (No. 2022JM-086). J. Yang thanks the Cyrus Tang Foundation (China) for Tang Scholar.

Author contributions

J.H.: Conceptualization, Methodology, Investigation, and Writing-original draft. B.L.: Conceptualization, Methodology, and Writing-Review&Editing. S.M.: Investigation, Validation, and Writing-Review&Editing. J.Y.: Conceptualization, Supervision, Visualization and Writing-Review&Editing. All authors reviewed the manuscript.

Competing interests

The authors declare no competing interests.

Additional information

Supplementary Information The online version contains supplementary material available at <https://doi.org/10.1038/s41598-022-11756-x>.

Correspondence and requests for materials should be addressed to S.M. or J.Y.

Reprints and permissions information is available at www.nature.com/reprints.

Publisher's note Springer Nature remains neutral with regard to jurisdictional claims in published maps and institutional affiliations.



Open Access This article is licensed under a Creative Commons Attribution 4.0 International License, which permits use, sharing, adaptation, distribution and reproduction in any medium or format, as long as you give appropriate credit to the original author(s) and the source, provide a link to the Creative Commons licence, and indicate if changes were made. The images or other third party material in this article are included in the article's Creative Commons licence, unless indicated otherwise in a credit line to the material. If material is not included in the article's Creative Commons licence and your intended use is not permitted by statutory regulation or exceeds the permitted use, you will need to obtain permission directly from the copyright holder. To view a copy of this licence, visit <http://creativecommons.org/licenses/by/4.0/>.

© The Author(s) 2022